ACS APPLIED MATERIALS & INTERFACES

www.acsami.org Research Article

Dihedral Restrained Molecular Dynamics Aligns Simulated and Experimental Crystallinity in Organic Solar Cells

Published as part of ACS Applied Materials & Interfaces special issue "Special Collection on the 115th Anniversary of Lanzhou University".

Wenkai Zhao, Ailin Li, Yecheng Zhou,* Zechen Hao, Jinhan Yang, Tianying Yan, Xiangjian Wan, Xiankai Chen, Yongsheng Chen,* and Guankui Long*

Cite This: ACS Appl. Mater. Interfaces 2025, 17, 45947−45957 Read Online

ACCESS | Metrics & More | Article Recommendations | Supporting Information

ABSTRACT: Organic solar cells (OSCs) present an efficient, low-cost alternative for renewable energy applications, with recent advancements driven by the development of nonfullerene acceptors (NFAs) that have significantly improved the power conversion efficiency (PCE) of OSCs to over 20%, narrowing the performance gap with other types of solar cells. The molecular stacking in the active layer is crucially important for highly efficient energy conversion; however, experimental techniques still face limitations in capturing the detailed structural information at the molecular level. To address this challenge, molecular dynamics (MD) simulations could provide atomistic insight into molecular configurations, offering opportunities to optimize the morphology in the active layer. Despite this, achieving experimentally accurate crystalline arrangements and domains within reasonable computational timeframes remains difficult. In this work, we have systematically investigated the influence of dihedral angle restraints in MD simulations based on the representative NFA, **CH17**, and **Y6**. It is found that dihedral restraints lead to more ordered molecular stacking with monomer, dimer, and long-range structures closely resembling the crystalline arrangements. Additionally, we confirmed that **CH17** exhibits stronger $\pi-\pi$ stackings compared to **Y6**, further validating its superior PCE. Our study highlights the important potential of dihedral angle restraints in improving the accuracy of molecular simulations, which offers valuable insights for the designing of high-performance OSC materials.

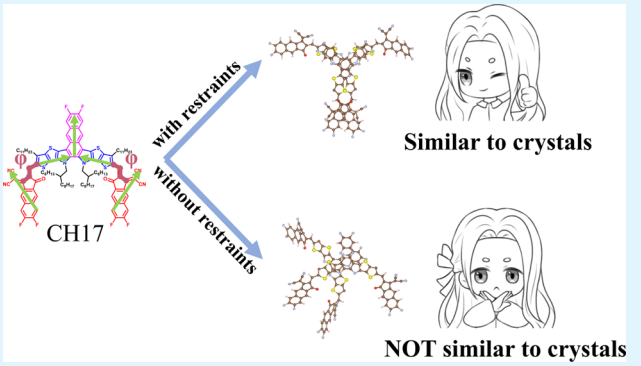

KEYWORDS: *organic solar cells, non-fullerene acceptors, molecular dynamics simulations, dihedral angle restraints, molecular stacking*

1. INTRODUCTION

Organic solar cells (OSCs) are considered as one of the most promising solutions for providing clean and renewable energy in various applications due to their unique advantages such as solution processing, low cost, lightweight, flexibility, and semitransparency.[1−4] Recently, the power conversion efficiency (PCE) of OSCs has surpassed 20%, significantly narrowing the efficiency gap with other solar cells.[4−6] This encouraging progress is primarily attributed to the rapid development of nonfullerene acceptors (NFAs).[7−9] These acceptors consist of fused-ring structures constructed from donor (D) and acceptor (A) units, featuring an A−DA′D−A structure.[10,11] The crystalline packing structure of NFA molecules within the active layer has been proven to play a crucial role in determining the fundamental optoelectronic properties relevant to OSCs, such as the electronic structure, absorption coefficient, exciton diffusion, exciton generation and dissociation, charge transport, collection and recombination, all of which ultimately influence the overall performance of OSC devices.[12−20] However, the current experimental techniques have not yet been capable of obtaining molecular-scale structural information. This technical limitation severely restricts research into a deep understanding of the relationship between molecular structure and device performance, becoming a bottleneck in advancing the development of OSCs.

To overcome this technical bottleneck, molecular dynamics (MD) simulations have been adopted as a valuable tool[21] since they can afford an atomistic depiction of the molecular stacking configurations within the active layer.[22] This capability not only facilitates the investigation of the material's internal structural information exceeding the limitations experimental

Received: May 2, 2025
Revised: July 22, 2025
Accepted: July 29, 2025
Published: August 5, 2025

https://doi.org/10.1021/acsami.5c08785
ACS Appl. Mater. Interfaces 2025, 17, 45947−45957

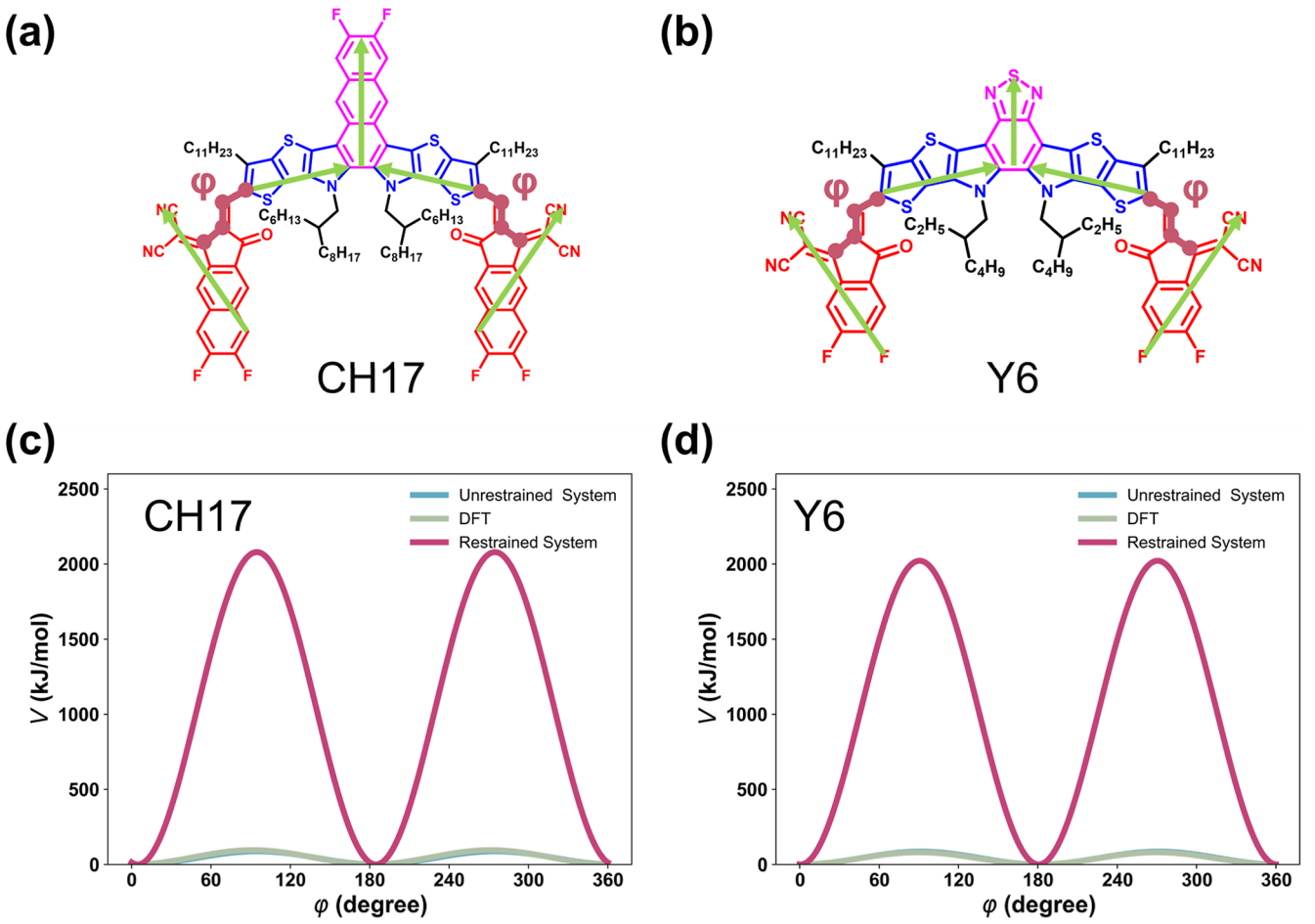

Figure 1. (a,b) Molecular structures of **CH17** (a) and **Y6** (b). The red region represents the **A** segment, the blue region represents the **D** segment, and the magenta region represents the **A′** segment. The green vectors indicate the principal axes of each segment, while the pink section highlights the dihedral angle connecting the **A** and **D** segments. (c,d) The dihedral barriers of **CH17** (c) and **Y6** (d) in the unrestrained system, restrained system, and calculated from DFT methods.

resolution but also reveals the detailed molecular arrangements in the active layer.[23−25] However, how to overcome the energy barriers to achieve experimentally accurate molecular structures of the active layer within a reasonable computational time frame during MD simulations remains a significant challenge.[26,27] This difficulty primarily stems from excessive rotation of the **A** segment, which disrupts the stacking configuration. Although the enhanced sampling techniques may help alleviate this issue to some extent, accurately identifying collective variables that fully capture the entire motion process remains a persistent challenge.[28−31]

Therefore, this study focused on the well-known NFA of **Y6**[32] and **CH17**,[33] with the latter notable for its extensive conjugated extensions, as the subjects of investigation. The molecular structures of these NFAs are shown in Figures 1a and 1b. We performed MD simulations on these molecules under conditions in which the dihedral angles connecting the **A** and **D** segments were either restrained or unrestrained. Our results demonstrate that by applying restraints on the dihedral angles, we can achieve monomer, dimer, and long-range structures that closely resemble the single crystals. Furthermore, morphological analysis demonstrates that **CH17** exhibits greater order and more extensive stacking than **Y6**, thereby revealing the reason why **CH17** shows superior properties compared to **Y6**. As a result, our work provides a straightforward approach in MD simulations to rapidly achieve rational stacking, offering a foundation for future design of OSC materials from the perspective of stacking structures.

2. EXPERIMENTAL SECTION

2.1. Computational Methods. All MD simulations were conducted utilizing the GROMACS (2023.3) software package, employing the GROMOS force field.[34] The restrained electrostatic potential (RESP) fitting technique was applied to derive partial charges for each molecule by using BDF software.[35−39]

The films were obtained from several stages of the isothermal−isobaric ensemble MD (*NPT*-MD). For the **CH17** system, 388 **CH17** molecules were randomly placed in a 50 × 50 × 50 nm^3 box. Similarly, for the **Y6** system, 496 **Y6** molecules were randomly placed in a 50 × 50 × 50 nm^3 box. The system initially underwent energy minimization, followed by a gradual annealing process from 1000 to 300 K over 300 ns. After a 100 ns equilibration phase, the production run lasted for 100 ns. Each system was simulated twice: once using restrained dihedral force constants and once using unrestrained dihedral force constants.

The LINCS algorithm was utilized to constrain covalent bonds involving hydrogen atoms.[40] A simulation time step of 1.0 fs was employed. Both the pressure and temperature were regulated using the Parrinello−Rahman barostat at 1 atm and the Nose−Hoover thermostat, respectively.[41,42] All analysis was performed on the frames extracted from the production run. The graphics were processed by the Visual Molecular Dynamics (VMD) program.[43] Analyses of molecular stacking were performed using the MDAnalysis Python library.[44]

https://doi.org/10.1021/acsami.5c08785
ACS Appl. Mater. Interfaces 2025, 17, 45947−45957

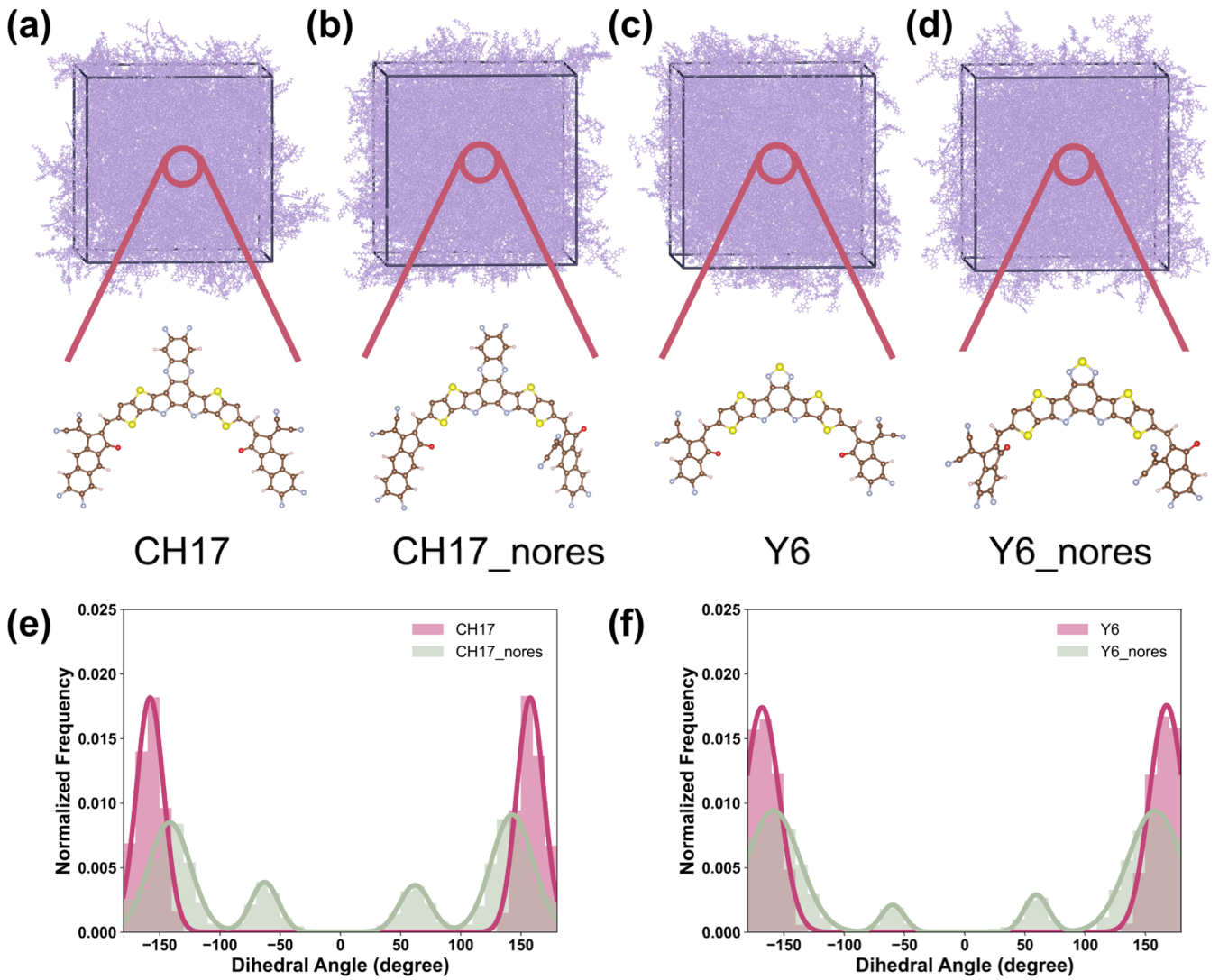

Figure 2. (a–d) Simulation results of the unrestrained and restrained **CH17** and **Y6** systems, along with randomly selected single-molecular structures. **CH17** and **Y6** represent the systems with dihedral angle restraints, while **CH17**_nores and **Y6**_nores represent the systems without dihedral angle restraints. (e,f) The dihedral angle distribution of **CH17** and **Y6** in the unrestrained and restrained systems.

The electronic coupling between dimers can be obtained by using MOMAP code.[45−48] To identify relevant molecular pairs for transfer integral calculations, we defined two monomers as forming a dimer if the distance between their nearest neighboring atoms is less than 6 Å. This distance-based criterion is commonly used to capture significant intermolecular interactions and has been shown to effectively identify relevant charge transport pathways. The transfer integrals between neighboring monomers were calculated using the code based on eq 1:[49]

$$V = \frac{H_{12} - \frac{1}{2}(H_{11} + H_{22})S}{1 - S^2} \quad (1)$$

Here, $H_{12} = \langle \psi_1 | H | \psi_2 \rangle$, $S = \langle \psi_1 | \psi_2 \rangle$, $H_{11} = \langle \psi_1 | H | \psi_1 \rangle$, $H_{12} = \langle \psi_2 | H | \psi_2 \rangle$, H is the Kohn−Sham Hamiltonian of the dimer, $\psi_{1/2}$ means the HOMO/LUMO of the monomer in the dimer for electron transport, and S is the overlap integral. We obtained the transfer integrals by using the density functional theory (DFT) at the B3LYP/6-31G(d) level.

2.2. The Method for Calculating the Overlap Area. First, for the source and target atom sets, the code performs principal component analysis (PCA). From the PCA results, the third principal component of the atom set (i.e., the direction with the smallest variance) is taken as the normal vector of the plane. Next, the atom sets are projected onto their respective PCA planes. Following this, the source atom set is projected onto the PCA plane of the target atom set, aligning both atom sets onto the same plane. Once the atom sets are on the same 3D plane, a PCA transformation is applied to obtain a 2D representation of both atom sets. Then, the convex hull function is used to calculate the convex hulls of the 2D representations of the source and target atom sets. The overlap area is determined by calculating the intersection of the convex hulls. Finally, the percentage of the intersection area relative to the convex hull area of the target atom set is computed. The final overlap area is the average of the overlap areas calculated by treating each atom set as both the source and the target. The actual computational results are shown in Figure S1.

2.3. The Method for Selecting Representative Stacking Configurations. For selecting representative stacking configurations, the input for clustering analysis included the segment center-of-mass (COM) distance (d), the dihedral angle between the two segment planes (φ), the angle between the long axes of the adjacent segment (θ), the molecule COM distance (d_m), and the overlap area (S_{12}). Clustering analysis was conducted using the Gaussian mixture model (GMM), and the results were visualized in 2D space through t-distributed stochastic neighbor embedding (t-SNE).

https://doi.org/10.1021/acsami.5c08785
ACS Appl. Mater. Interfaces 2025, 17, 45947−45957

To determine the optimal number of clusters, two evaluation metrics were employed: the Bayesian information criterion (BIC) and the silhouette score, along with a penalty function.

$$\text{Score} = \text{normalized silhouette} - \text{normalized BIC} - \text{cluster penalty weight} \times \text{number of clusters}$$

This approach considered not only the goodness of fit of the model (using BIC) but also the quality of the clustering (using the silhouette score) while preventing overclustering through the penalty function. The relationship between the actual scores and the number of clusters is shown in Figure S2, and the *t*-SNE visualization is presented in Figure S3.

The representative dimer within each cluster was selected as the sample closest to the center of the Gaussian distribution for that cluster.

3. RESULTS AND DISCUSSION

The accuracy of MD simulation results largely depends on the selection of force field parameters. Among these, dihedral angle parameters have a particularly significant impact on monomer structures, directly influencing the molecular torsion and packing behavior and therefore playing a critical role in the precision of the simulation results. To ensure the reliability of the simulations, it is essential to carefully choose and optimize the dihedral angle parameters. This is especially true when studying the complicated molecular systems, such as highly conjugated NFAs, where the variations in dihedral angles can profoundly influence the packing characteristics of the entire system. Properly setting the dihedral angle parameters allows for better reproduction of the experimental results, thus providing more accurate theoretical guidance for material design and performance optimization. To investigate the influence of restraining dihedral angles on the final simulation results, the following dihedral potential function was applied for the angles connecting segments **A** and **D** (as shown in Figure 1a,b).

$$V(\phi) = k_\phi(1 + \cos(n\phi - \phi_s)) \quad (2)$$

where V is the dihedral energy, k_ϕ is the force constant associated with the dihedral potential, n is the periodicity of the dihedral, ϕ is the dihedral angle, and ϕ_s is the equilibrium dihedral angle.

Two different force constant specifications were employed. The first force constant was obtained by fitting the results calculated using DFT with the BDF software,[35−39] labeled as the "unrestrained system". The force constants for **CH17** and **Y6** were 44 and 42 kJ/mol, respectively. The second was the DFT-calculated force constant with an additional 1000 kJ/mol, labeled as the "restrained system". The force constants for **CH17** and **Y6** were 1039 and 1010 kJ/mol, respectively. Although the additional force constant was nominally set to 1000, the final values are not strictly equal to the original plus 1000, as the "+1000" is an ideal target value, but the actual results may deviate slightly due to the coupling effects in the force field model. The dihedral barriers of **CH17** and **Y6** in the unrestrained system, the restrained system, and those calculated from quantum chemistry methods are shown in Figures 1c and 1d. The potential barrier of the dihedral angle in **CH17**, without any restraint, is higher than that of **Y6**, indicating that **CH17** exhibits stronger rigidity. As expected, the enhanced molecular planarity and rigidity of **CH17** result in a smaller reorganization energy of 126 meV, compared to 148 meV for **Y6**. This also explains why **CH17** exhibits superior optoelectronic performance compared to **Y6**.

MD simulations were then performed on the **CH17** and **Y6** systems, with the detailed simulation procedures provided in the Supporting Information. The simulated results are illustrated in Figure 2a−d. Initially, the distribution of the dihedral angles was analyzed, as shown in Figures 2e and 2f and Table S1. The results demonstrated that introducing the restrained potential successfully confined the dihedral angles within a specific range, validating the effectiveness of this strategy in preventing the excessive rotational freedom. Furthermore, the individual molecular structures were randomly extracted from the simulated film (as shown in Figure 2a−d, the alkyl chains were omitted for clarity), and it was found that both **Y6** and **CH17** in the restrained conditions appeared flatter and more similar to the single-molecular conformations observed in single crystals.[33,50] To further quantitatively assess the differences of single-molecule conformations between the system with and without restraint, the root-mean-square deviation (RMSD) of the individual molecules from MD simulations compared to those in single crystals was calculated. Generally, a smaller RMSD value indicates higher similarity between two structures. As shown in Table 1, the RMSD values of both the **CH17** and **Y6** systems were significantly lower in the presence of the restraints, aligning with the greater resemblance to the molecular conformations in single crystals. This confirms that applying restraints to the key dihedral angles effectively reduces the conformational flexibility, resulting in molecular structures that more closely mimic the crystalline state. Simultaneously, it was observed that the **CH17** system exhibited a greater reduction in RMSD upon applying restraints compared to that of the **Y6** system. This greater decrease may be attributed to the larger molecular size of **CH17**'s **A** segment, as imposing restraints on this segment appears to have a more pronounced impact on the overall system.

Table 1. RMSD Values of the Restrained and Unrestrained CH17 and Y6 Systems

	RMSD (Å)
CH17	1.36
CH17_nores	1.98
Y6	1.45
Y6_nores	1.82

To further confirm that the system with applied restraints more closely resembles the experimental system, we further simulated the grazing-incidence wide-angle X-ray scattering (GIWAXS) of both systems with and without a restraint. The experimental[33] and simulated GIWAXS patterns are shown in Figure 3a, and Table S2 presents the corresponding line-cut profiles, $\pi-\pi$ stacking distance, and crystal coherence length (CCL). Since no substrate was included in the simulation, the simulated GIWAXS patterns could not distinguish the face-on or edge-on packings. As a result, the GIWAXS patterns obtained from the simulation exhibit a random distribution. However, the stacking distance and CCL can still be compared with the experimental data. Therefore, we employed the overall average value to compare the simulated results with the experimental in-plane (IP) and out-of-plane (OOP) data. As shown in Figure 3b, it is clear that after applying the dihedral angle restraints, the peak positions align more closely with the

https://doi.org/10.1021/acsami.5c08785
ACS Appl. Mater. Interfaces 2025, 17, 45947−45957

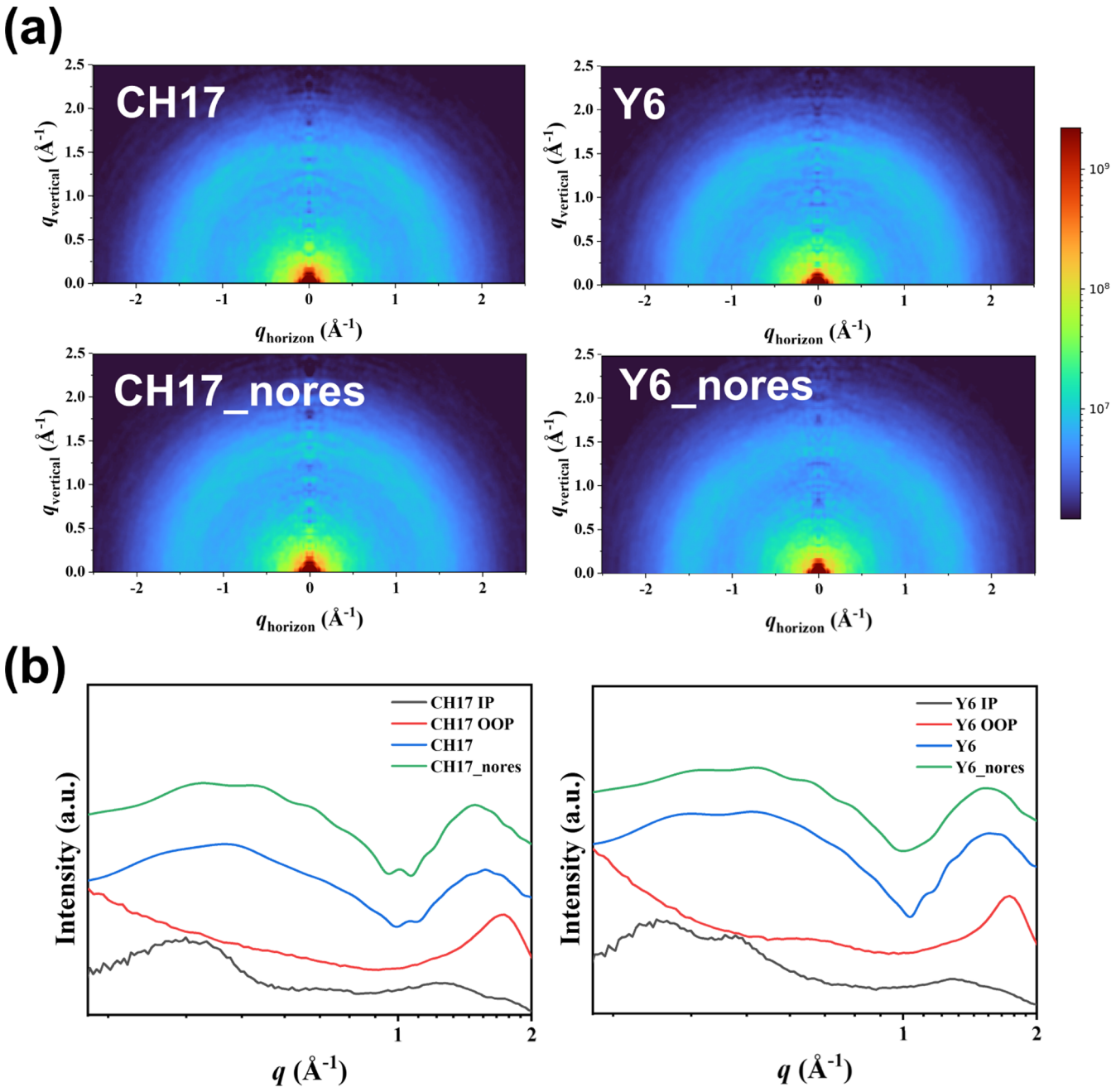

Figure 3. (a) The simulated 2D GIWAXS patterns of **CH17** and **Y6** with and without restraints. (b) Line-cut profiles extracted from 2D GIWAXS. The black and red lines represent the experimental in-plane (IP) and out-of-plane (OOP) data,[33] while the blue and green lines correspond to the simulated values with and without restraints, respectively.

experimental results. It is clear that after applying the dihedral angle restraints, the peak positions align more closely with the experimental results. This indicates that the introduction of dihedral angle restraints results in more ordered stacking, enhancing the consistency with the experimental data. Moreover, the impact of the restraints is particularly significant in the region below 1 Å^{-1}. In the unrestrained **CH17** and **Y6** systems, several peaks are observed in this region. However, after the dihedral angle restraints are applied, the number of peaks decreases, and the resulting pattern is in better agreement with the experimental data. The comparison between the simulated and experimental GIWAXS patterns highlights the effectiveness of these restraints in improving the accuracy of the model and enhancing the correspondence between the theoretical results and experimental data.

Moving forward, the impact of restrained dihedral angles on the stacking behavior within the films was further explored. **CH17** and **Y6** were segmented into three segments, labeled as **A**, **D**, and **A′**, resulting in the establishment of six distinct stacking modes. The radial distribution functions (RDFs, $g(r)$) were calculated for each of the stacking modes, both with and without the restraints. As depicted in Figure 4, the RDFs exhibit the probability of finding a particle at a certain distance from a reference particle, with higher $g(r)$ peaks indicating a greater stacking density at specific distances. The $\pi-\pi$ stacking peaks observed in the RDFs (ranging from 3.8 to 4.0 Å) varied significantly among the different systems. Notably, systems

https://doi.org/10.1021/acsami.5c08785
ACS Appl. Mater. Interfaces 2025, 17, 45947−45957

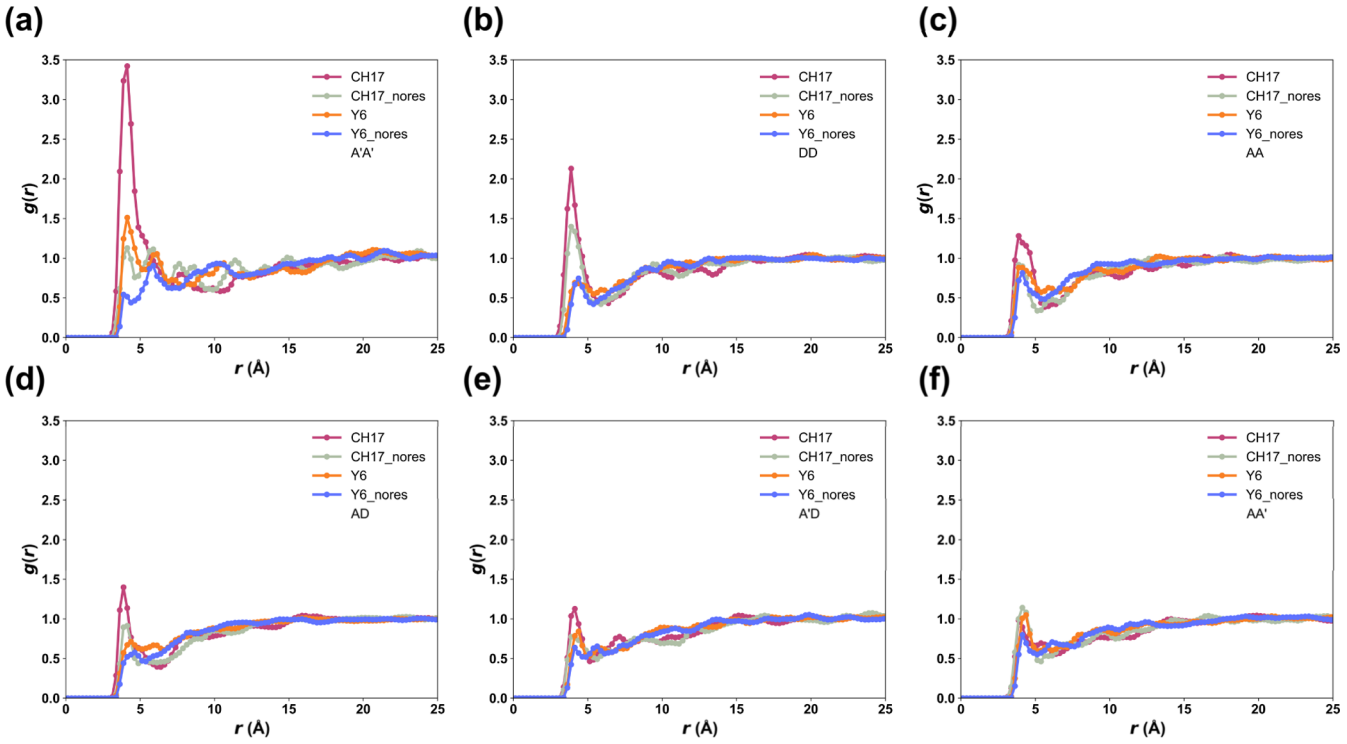

Figure 4. (a–f) Radial distribution function ($g(r)$) for the different stacking modes of **CH17** and **Y6**, with and without restraints: **A′A′** (a), **DD** (b), **AA** (c), **AD** (d), **A′D** (e), and **AA′** (f).

with the applied restraints generally exhibit higher $\pi-\pi$ stacking peaks than those without, suggesting that the restraints lead to more ordered stacking. This was particularly obvious in the **A′A′** and **DD** stacking modes, where the restrained **CH17** exhibits significantly higher peaks compared to the unrestrained system, indicating that the restraints facilitate the formation of more crystalline-like morphology within the same simulation time frame, thereby reaffirming the effectiveness of this strategy. However, for the **AA′** stacking mode with the applied restraints, the peak heights were comparable to those without. This may be attributed to the restraints hindering the rotation of segment **A**, making it more challenging for segment **A** to stack via segment **A′** directionally, and consequently, the introduction of the restraints does not significantly influence the peak heights. Additionally, it is found that in the **CH17** system, regardless of whether restraints were applied or not, most of the stacking modes continue to exhibit the $\pi-\pi$ stacking peaks, which are higher than those in the **Y6** system. Notably, for the **A′A′** stacking mode, the $\pi-\pi$ stacking peak in the restrained **CH17** system was nearly three times higher than that in the restrained **Y6** system. This suggests that the simultaneous conjugated extension of both the central core and the terminal groups in **CH17** leads to a more orderly stacking structure. This improved organization may promote superior electronic interactions within the molecule, potentially enhancing its performance in optoelectronic applications.

In order to gain more comprehensive insight into the two different models developed in this study, an in-depth investigation of the dimer configurations formed by two adjacent molecules was further conducted. We define a dimer as two molecules with a nearest atomic distance (d_n) of less than 7 Å. This characterization was based on four critical parameters: the distance between the centers of mass (COM) of the adjacent molecular backbones (d), the dihedral angle between the planes of two adjacent molecules (φ), the angle between the long axes of the adjacent molecules (θ), and the overlap area between them (S_{12}). S_1 is the projection of molecule 1 onto molecule 2, and S_2 is the projection of molecule 2 onto molecule 1. The overlap area S_{12} is then the average of S_1 and S_2. These parameters are schematically illustrated in Figure 5a. Density heatmaps of $d-\varphi-S_{12}$ are also shown in Figures S4–S7, where areas in purple indicate a higher density of occurrences, and pink areas denote a lower density. An arrangement is considered face-on when two adjacent molecules have face-to-face orientations between their backbones, characterized by φ being less than 30°, d being less than 0.8 nm, and S_{12} being larger than 0.4. This corresponds to the area near the bottom-left corner at the top of the diagram. Typically, a face-on orientation promotes the most robust parallel $\pi-\pi$ stacking interactions, resulting in the enhanced electronic coupling, which is indicative of an improved charge transfer rate. Therefore, upon imposing the restraints, the number of $\pi-\pi$ stacking interactions became more concentrated in the face-on regions. This pattern suggests that targeted restraints can effectively enhance the molecular orientation, thereby more accurately replicating real systems.

To perform quantitative analysis, both the total number of stackings within each system and the number that conform to the face-on orientation were further calculated, as shown in Figures 5b and 5c. In terms of the overall stacking, it is clear that the **AA**, **AD**, and **AA′** stacking modes are more prevalent than other modes. Thus, focusing on modifications to the **A** segment of the molecule could significantly influence the stacking behavior, offering a valuable strategy for future molecular design. Furthermore, for the **AA**, **AD**, and **AA′** stacking conditions, the imposition of restraints reduced the total numbers of stackings. This reduction is likely due to the

https://doi.org/10.1021/acsami.5c08785
ACS Appl. Mater. Interfaces 2025, 17, 45947–45957

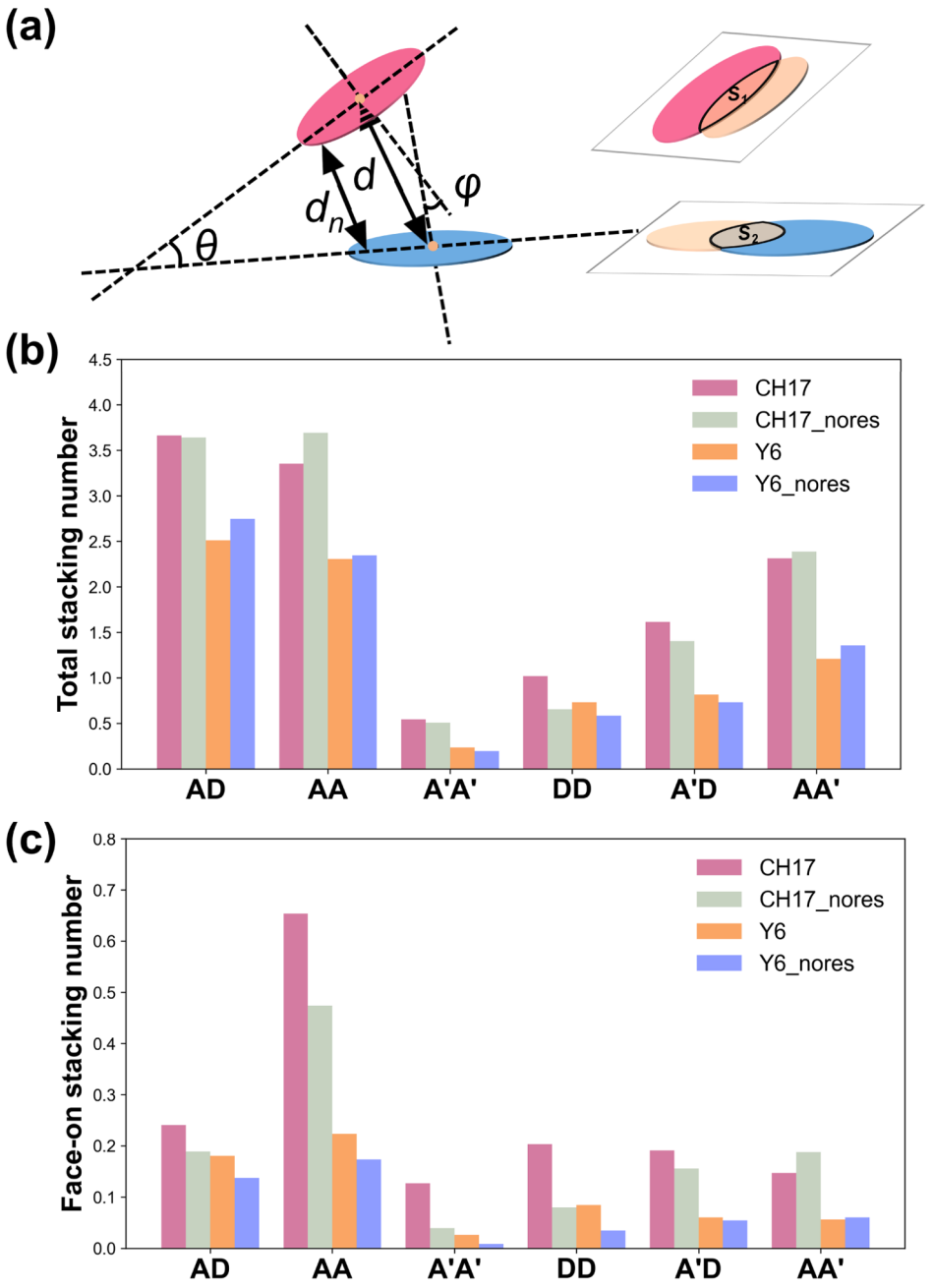

Figure 5. (a) Five selected geometric parameters of different dimer configurations: segment COM distance (d), dihedral angle between the planes of two adjacent molecules (φ), angle between the long axes (θ), nearest atomic distance between the two segments (d_n), and the overlap area (S_{12}) of the two adjacent molecules. S_1 is the projection of molecule 1 onto molecule 2, and S_2 is the projection of molecule 2 onto molecule 1. The overlap area S_{12} is then the average of S_1 and S_2. (b) Total stacking number per unit volume for the restrained and unrestrained **CH17** and **Y6** systems. (c) Face-on stacking number per unit volume for the restrained and unrestrained **CH17** and **Y6** systems.

restraints on the **A** segment, which limit its free rotation and alignment with other components. In contrast, for other stacking modes, the introduction of restraints led to an increase in the stacking numbers. This increase can be attributed to the restraints on the **A** segment, which make the molecule more planar, thereby reducing steric hindrance and promoting more $\pi-\pi$ stacking. To support this hypothesis, we further calculated the molecular planarity within the films was further calculated. The molecular planarity parameter (MPP) is defined as the root-mean-square deviation of each atom from the best-fit plane of the investigated molecule, and the span of deviation from plane (SDP) represents the range between the highest and lowest deviations of all considered atoms from a reference plane. Notably, alkyl chains and hydrogen atoms were excluded from this analysis. Therefore, smaller MPP and SDP indicate enhanced planarity. The MPP and SDP values of the four investigated systems were calculated and are summarized in Table 2. It is found that for the restrained **Y6** and **CH17** systems, both MPP and SDP values are much smaller, indicating better overall molecular planarity. This observation further supports the hypothesis as mentioned above. It is also found that for the face-on stacking, nearly all stacking modes exhibit a higher stacking number in the restrained systems compared to the unrestrained ones. This may also be linked to

https://doi.org/10.1021/acsami.5c08785
ACS Appl. Mater. Interfaces 2025, 17, 45947−45957

Table 2. MPP and SDP Values of the Restrained and Unrestrained CH17 and Y6 Systems

	MPP (Å)	SDP (Å)
CH17	0.95	5.45
CH17_nores	1.32	7.09
Y6	0.78	4.37
Y6_nores	1.05	5.62

the aforementioned enhancement of molecular planarity, which promotes the tighter and more ordered molecular stackings. The application of restraints therefore promotes the molecules in the system to adopt more regular stacking patterns, further validating the positive impact of dihedral restraints on stacking behaviors. Additionally, as shown in Figure 5c, both the restrained and unrestrained systems demonstrate that the total stacking numbers and face-on stacking numbers in **CH17** are significantly larger than those in the **Y6** system. This further confirms that the extension of multiple conjugations to the central and terminal units in **CH17** greatly enhances the intermolecular packings. Such an increase in the stacking number could improve the charge transport, which is essential for boosting the overall efficiency of OSCs.

To elucidate the types of dimer configurations present in the various films and better assess the differences among them, the GMM was also utilized as a clustering method, with the workflow shown in Figure 6a. Clustering was performed by using all parameters listed in Figure 5a, except for d_n, and additionally incorporating d_m. By analyzing the clustering distribution centers (i.e., the means of the Gaussian distributions), we can identify the characteristics of each dimer configuration, providing a more precise description of the variations in the dimer stackings within the film. This method quantifies the types of dimers observed in the MD-simulated films.

As shown in Figures S8−S14, the number of clusters derived for each stacking condition, along with detailed information about each dimer, is summarized. An increase in the number of clusters suggests a greater variety of stacking modes, indicating more complex and diverse stacking structures within the films. For **CH17** and **Y6**, most stacking configurations show that the number of clusters increases with the introduction of restraints, such as the **AD**, **DD**, and **A′D** configurations for **CH17** and the **A′D** and **AA′** configurations for **Y6**. However, for **CH17**'s **AA′** configuration and **Y6**'s **A′A′**, **AA**, and **DD** configurations, the number of clusters decreases. The number of clusters for the remaining stacking configurations is unaffected by the introduction of restraints. The effect of adding restraints to the stacking can be understood in two ways. The increase in the number of clusters could be attributed to the fact that when the rotation in part **A** is restricted, it becomes more difficult for the molecules to stack with each other. On the other hand, the decrease in the number of clusters suggests that the introduction of restraints alleviates the increase in molecular configurations caused by the rotation in part **A**, leading to a more uniform and orderly stacking arrangement. The unchanged number of clusters may result from a balance between the two opposing effects. The different behaviors observed for **CH17** and **Y6** demonstrate that the introduction of restraints has varying effects on the stacking configurations of different molecules, highlighting that the role of part **A** in the stacking behavior of different molecules may not be entirely the same.

After the typical dimer of every stacking mode was identified, a detailed analysis was further conducted. As shown in Figure 6b, the application of restraints on the dihedral angles results in a typical **CH17** dimer that closely

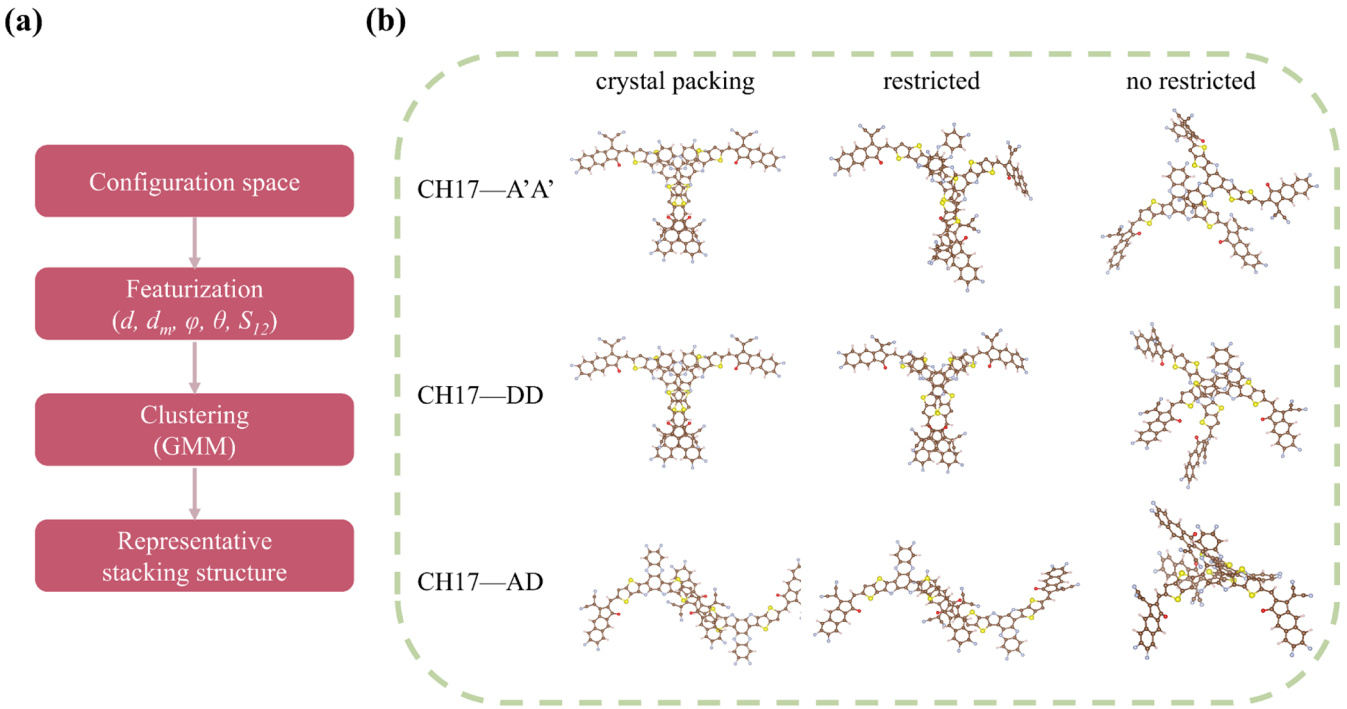

Figure 6. (a) Workflow for quantifying the typical dimers in molecular dynamics simulations. (b) Comparison of typical dimers in **CH17** crystal packing[33] with those from restrained and unrestrained simulated systems.

https://doi.org/10.1021/acsami.5c08785
ACS Appl. Mater. Interfaces 2025, 17, 45947−45957

resembles a crystalline arrangement. This validates the effectiveness of our strategy and underscores the potential of restrained dihedral angles in improving the molecular organization within the system. This approach offers valuable insights for further studies on material stacking behavior and opens new avenues for exploring more efficient molecular stacking strategies.

To further analyze the long-range order in each system, the ordered connection was then calculated. An ordered connection is defined as any segment of the molecule in a face-on stacking mode overlapping with any segment of the adjacent molecule and then sequentially continuing to stack until no further segment of any molecules can form a face-on stacking interaction with the nearest molecules. By analyzing these ordered connections, the structural characteristics of the system can be further evaluated. Based on this definition, the number and length of ordered connections in each box were quantified, thereby assessing the long-range order of the system. As shown in Figure S15, in systems with restrained dihedral angles, the number of the ordered connections significantly increased, indicating that molecular arrangement became more orderly. Additionally, the transfer integrals for the longest ordered connection in each system were calculated using MOMAP and BDF, and they are presented in Figures 7 and S16. The results showed that the transfer integrals were larger in systems with restrained dihedral angles, indicating tighter intermolecular packing. This further validates the effectiveness of our strategy in MD simulations for achieving crystalline packing structure within the limited time scales. With further optimization, this strategy has the potential to be even more applicable and effective across different material systems.

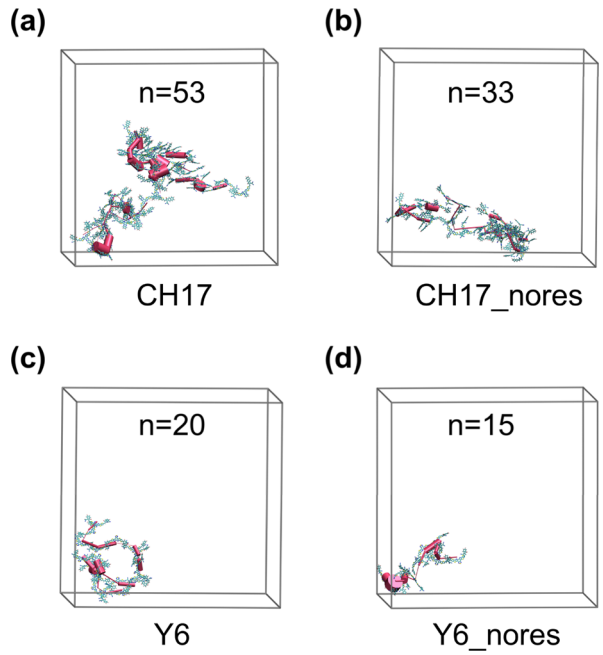

Figure 7. (a–d) The longest ordered connection in the restrained and unrestrained **CH17** (a,b) and **Y6** (c,d) systems. The electron transfer integrals between each pair of dimers are represented by pink cylinders. The centers of the top and bottom surfaces of the cylinders are connected to the centers of mass of the molecules, with the thickness of the cylinders indicating the magnitude of the electron transfer integrals. The thicker the cylinder, the larger the transfer integral.

Meanwhile, regardless of the inclusion of dihedral restraints, the number and length of the ordered connections in the **CH17** system were much larger than those in the **Y6** system. Additionally, the transfer integrals in the **CH17** system were much higher than those in the **Y6** system. This further confirms that **CH17**, due to its extended conjugation structure, exhibits a clear advantage in intermolecular packing and charge transport. These advantages enable **CH17** to form more ordered and stable packing patterns, resulting in superior charge transport properties.

4. CONCLUSIONS

In this study, we have systematically investigated the influence of dihedral angle restraints in MD simulations on the stacking behavior of OSC materials, specifically focusing on the representative NFA of **CH17** and **Y6**. By imposing the dihedral restraints, we achieved monomer, dimer, and long-range structures that closely resembled their crystalline states, thereby enhancing the accuracy of our simulations. Our findings demonstrate that restrained dihedral angles significantly improve the molecular planarity, reduce the conformational flexibility, and thus promote the ordered $\pi-\pi$ stacking, ultimately resulting in packing structures that closely resemble the crystalline arrangements. Furthermore, we found that, compared with **Y6**, **CH17** exhibits extended conjugation at both the central core and end unit, resulting in a greater stacking number, demonstrating superior stacking behavior, consistent with its excellent PCE. However, while restraining the dihedral angles made the simulation results more realistic, simulations without dihedral restraints were still able to capture the correct overall trends. In conclusion, our methodology offers a straightforward and effective strategy for simulating realistic molecular packing structures in OSCs, providing a pathway for the future design of efficient OSC molecules.

■ ASSOCIATED CONTENT

Supporting Information

The Supporting Information is available free of charge at https://pubs.acs.org/doi/10.1021/acsami.5c08785.

Molecular dynamics simulation methods, clustering results with structural data, and corresponding simulation GIWAXS data for **CH17** and **Y6** systems (PDF)

■ AUTHOR INFORMATION

Corresponding Authors

Yecheng Zhou − *School of Materials Science & Engineering, Sun Yat-sen University, Guangzhou 510006, China;* orcid.org/0000-0001-8222-7193; Email: zhouych29@mail.sysu.edu.cn

Yongsheng Chen − *The Centre of Nanoscale Science and Technology and Key Laboratory of Functional Polymer Materials, Institute of Polymer Chemistry, Renewable Energy Conversion and Storage Center (RECAST), College of Chemistry, Nankai University, Tianjin 300071, China;* orcid.org/0000-0003-1448-8177; Email: yschen99@nankai.edu.cn

Guankui Long − *Frontiers Science Center for New Organic Matter, Tianjin Key Lab for Rare Earth Materials and Applications, Renewable Energy Conversion and Storage*

https://doi.org/10.1021/acsami.5c08785
ACS Appl. Mater. Interfaces 2025, 17, 45947−45957

Center (RECAST), School of Materials Science and Engineering, National Institute for Advanced Materials, Nankai University, Tianjin 300350, China; orcid.org/0000-0002-1826-3736; Email: longgk09@nankai.edu.cn

Authors

Wenkai Zhao − *Frontiers Science Center for New Organic Matter, Tianjin Key Lab for Rare Earth Materials and Applications, Renewable Energy Conversion and Storage Center (RECAST), School of Materials Science and Engineering, National Institute for Advanced Materials, Nankai University, Tianjin 300350, China*

Ailin Li − *College of Science, Civil Aviation University of China, Tianjin 300300, China*

Zechen Hao − *Frontiers Science Center for New Organic Matter, Tianjin Key Lab for Rare Earth Materials and Applications, Renewable Energy Conversion and Storage Center (RECAST), School of Materials Science and Engineering, National Institute for Advanced Materials, Nankai University, Tianjin 300350, China*

Jinhan Yang − *Frontiers Science Center for New Organic Matter, Tianjin Key Lab for Rare Earth Materials and Applications, Renewable Energy Conversion and Storage Center (RECAST), School of Materials Science and Engineering, National Institute for Advanced Materials, Nankai University, Tianjin 300350, China*

Tianying Yan − *Frontiers Science Center for New Organic Matter, Tianjin Key Lab for Rare Earth Materials and Applications, Renewable Energy Conversion and Storage Center (RECAST), School of Materials Science and Engineering, National Institute for Advanced Materials, Nankai University, Tianjin 300350, China;* orcid.org/0000-0002-2708-7906

Xiangjian Wan − *The Centre of Nanoscale Science and Technology and Key Laboratory of Functional Polymer Materials, Institute of Polymer Chemistry, Renewable Energy Conversion and Storage Center (RECAST), College of Chemistry, Nankai University, Tianjin 300071, China;* orcid.org/0000-0001-5266-8510

Xiankai Chen − *Institute of Functional Nano & Soft Materials (FUNSOM), Soochow University, Suzhou, Jiangsu 215123, China;* orcid.org/0000-0002-8580-7246

Complete contact information is available at: https://pubs.acs.org/10.1021/acsami.5c08785

Author Contributions

The manuscript was written through contributions of all authors. All authors have given approval to the final version of the manuscript.

Notes

The authors declare no competing financial interest.

ACKNOWLEDGMENTS

The authors gratefully acknowledge the financial support from the NSFC (Grant Numbers: 52103218, 52473305, 92256202, 12261131500) of China, the Fundamental Research Funds for the Central Universities, Nankai University (Grant Number: 023-63233038), the 111 Project (B18030), and the Supercomputing Center of Lanzhou University. The authors also acknowledge HZWTECH for providing computation facilities.

REFERENCES

(1) Zhao, Y.; Li, Z.; Deger, C.; Wang, M.; Peric, M.; Yin, Y.; Meng, D.; Yang, W.; Wang, X.; Xing, Q.; Chang, B.; Scott, E. G.; Zhou, Y.; Zhang, E.; Zheng, R.; Bian, J.; Shi, Y.; Yavuz, I.; Wei, K.-H.; Houk, K. N.; Yang, Y. Achieving sustainability of greenhouses by integrating stable semi-transparent organic photovoltaics. *Nat. Sustain.* **2023**, *6* (5), 539−548.

(2) Wang, Y.; Xue, J.; Zhong, H.; Everett, C. R.; Jiang, X.; Reus, M. A.; Chumakov, A.; Roth, S. V.; Adedeji, M. A.; Jili, N.; Zhou, K.; Lu, G.; Tang, Z.; Mola, G. T.; Müller-Buschbaum, P.; Ma, W. Control of the Crystallization and Phase Separation Kinetics in Sequential Blade-Coated Organic Solar Cells by Optimizing the Upper Layer Processing Solvent. *Adv. Energy Mater.* **2023**, *13* (7), 2203496.

(3) Zhao, H.; Lin, B.; Xue, J.; Naveed, H. B.; Zhao, C.; Zhou, X.; Zhou, K.; Wu, H.; Cai, Y.; Yun, D.; Tang, Z.; Ma, W. Kinetics Manipulation Enables High-Performance Thick Ternary Organic Solar Cells via R2R-Compatible Slot-Die Coating. *Adv. Mater.* **2022**, *34* (7), 2105114.

(4) Liao, C.-Y.; Chen, Y.; Lee, C.-C.; Wang, G.; Teng, N.-W.; Lee, C.-H.; Li, W.-L.; Chen, Y.-K.; Li, C.-H.; Ho, H.-L.; Tan, P.; Wang, B.; Huang, Y.-C.; Young, R.; Wasielewski, M.; Marks, T.; Chang, Y.-M.; Facchetti, A. Processing strategies for an organic photovoltaic module with over 10% efficiency. *Joule* **2020**, *4* (1), 189−206.

(5) Chen, H.; Huang, Y.; Zhang, R.; Mou, H.; Ding, J.; Zhou, J.; Wang, Z.; Li, H.; Chen, W.; Zhu, J.; Cheng, Q.; Gu, H.; Wu, X.; Zhang, T.; Wang, Y.; Zhu, H.; Xie, Z.; Gao, F.; Li, Y.; Li, Y. Organic solar cells with 20.82% efficiency and high tolerance of active layer thickness through crystallization sequence manipulation. *Nat. Mater.* **2025**, *24* (3), 444−453.

(6) Wang, L.; Chen, C.; Gan, Z.; Cheng, J.; Sun, Y.; Zhou, J.; Xia, W.; Liu, D.; Li, W.; Wang, T. Diluted Ternary Heterojunctions to Suppress Charge Recombination for Organic Solar Cells with 21% Efficiency. *Adv. Mater.* **2025**, *37* (13), 2419923.

(7) Lin, Y.; Wang, J.; Zhang, Z. G.; Bai, H.; Li, Y.; Zhu, D.; Zhan, X. An Electron Acceptor Challenging Fullerenes for Efficient Polymer Solar Cells. *Adv. Mater.* **2015**, *27* (7), 1170−1174.

(8) Zheng, Z.; Wang, J.; Bi, P.; Ren, J.; Wang, Y.; Yang, Y.; Liu, X.; Zhang, S.; Hou, J. Tandem organic solar cell with 20.2% efficiency. *Joule* **2022**, *6* (1), 171−184.

(9) Holliday, S.; Ashraf, R. S.; Nielsen, C. B.; Kirkus, M.; Röhr, J. A.; Tan, C.-H.; Collado-Fregoso, E.; Knall, A.-C.; Durrant, J. R.; Nelson, J.; McCulloch, I. A rhodanine flanked nonfullerene acceptor for solution-processed organic photovoltaics. *J. Am. Chem. Soc.* **2015**, *137* (2), 898−904.

(10) Cui, Y.; Xu, Y.; Hou, J. High efficiency and more functions bring a bright future for organic photovoltaic cells. *Sci. Bull.* **2022**, *67* (13), 1300−1303.

(11) Yi, J.; Zhang, G.; Yu, H.; Yan, H. Advantages, challenges and molecular design of different material types used in organic solar cells. *Nat. Rev. Mater.* **2024**, *9* (1), 46−62.

(12) Kim, J. H.; Schembri, T.; Bialas, D.; Stolte, M.; Würthner, F. Slip-Stacked J-Aggregate Materials for Organic Solar Cells and Photodetectors. *Adv. Mater.* **2022**, *34* (22), 2104678.

(13) Li, W.; Chen, M.; Cai, J.; Spooner, E. L.; Zhang, H.; Gurney, R. S.; Liu, D.; Xiao, Z.; Lidzey, D. G.; Ding, L.; Wang, T. Molecular order control of non-fullerene acceptors for high-efficiency polymer solar cells. *Joule* **2019**, *3* (3), 819−833.

(14) Mai, J.; Xiao, Y.; Zhou, G.; Wang, J.; Zhu, J.; Zhao, N.; Zhan, X.; Lu, X. Hidden Structure Ordering Along Backbone of Fused-Ring Electron Acceptors Enhanced by Ternary Bulk Heterojunction. *Adv. Mater.* **2018**, *30* (34), 1802888.

(15) Perdigón-Toro, L.; Phuong, L. Q.; Eller, F.; Freychet, G.; Saglamkaya, E.; Khan, J. I.; Wei, Q.; Zeiske, S.; Kroh, D.; Wedler, S.; Köhler, A.; Armin, A.; Laquai, F.; Herzig, E. M.; Zou, Y.; Shoaee, S.; Neher, D. Understanding the Role of Order in Y-Series Non-Fullerene Solar Cells to Realize High Open-Circuit Voltages. *Adv. Energy Mater.* **2022**, *12* (12), 2103422.

(16) Ye, L.; Weng, K.; Xu, J.; Du, X.; Chandrabose, S.; Chen, K.; Zhou, J.; Han, G.; Tan, S.; Xie, Z.; Yi, Y.; Li, N.; Liu, F.; Hodgkiss, J.

M.; Brabec, C. J.; Sun, Y. Unraveling the influence of non-fullerene acceptor molecular packing on photovoltaic performance of organic solar cells. *Nat. Commun.* **2020**, *11*, 6005.
(17) Zhang, G.; Chen, X.-K.; Xiao, J.; Chow, P. C. Y.; Ren, M.; Kupgan, G.; Jiao, X.; Chan, C. C. S.; Du, X.; Xia, R.; Chen, Z.; Yuan, J.; Zhang, Y.; Zhang, S.; Liu, Y.; Zou, Y.; Yan, H.; Wong, K. S.; Coropceanu, V.; Li, N.; Brabec, C. J.; Bredas, J.-L.; Yip, H.-L.; Cao, Y. Delocalization of exciton and electron wavefunction in non-fullerene acceptor molecules enables efficient organic solar cells. *Nat. Commun.* **2020**, *11*, 3943.
(18) Zhang, X.; Li, C.; Xu, J.; Wang, R.; Song, J.; Zhang, H.; Li, Y.; Jing, Y.-N.; Li, S.; Wu, G.; Zhou, J.; Li, X.; Zhang, Y.; Li, X.; Zhang, J.; Zhang, C.; Zhou, H.; Sun, Y.; Zhang, Y. High fill factor organic solar cells with increased dielectric constant and molecular packing density. *Joule* **2022**, *6* (2), 444−457.
(19) Han, G.; Hu, T.; Yi, Y. Reducing the Singlet-Triplet Energy Gap by End-Group π-π Stacking Toward High-Efficiency Organic Photovoltaics. *Adv. Mater.* **2020**, *32* (22), 2000975.
(20) Han, G.; Yi, Y. Molecular Insight into Efficient Charge Generation in Low-Driving-Force Nonfullerene Organic Solar Cells. *Acc. Chem. Res.* **2022**, *55* (6), 869−877.
(21) Kupgan, G.; Chen, X.-K.; Brédas, J.-L. Molecular packing of non-fullerene acceptors for organic solar cells: Distinctive local morphology in Y6 vs. ITIC derivatives. *Mater. Today Adv.* **2021**, *11*, 100154.
(22) Cho, E.; Risko, C.; Kim, D.; Gysel, R.; Cates, N.; Breiby, D. W.; McGehee, M. D.; Toney, M. F.; Kline, R. J.; Bredas, J.-L. Three-dimensional packing structure and electronic properties of biaxially oriented poly (2, 5-bis (3-alkylthiophene-2-yl) thieno [3, 2-b] thiophene) films. *J. Am. Chem. Soc.* **2012**, *134* (14), 6177−6190.
(23) Wang, J.; Chen, T.; Zhao, W.; Tang, X.; Bai, Y.; Zhou, W.; Long, G.; Ji, X.; Lu, G.; Feng, W.; Wan, X.; Kan, B.; Chen, Y. Effective Regulation of Morphologies and Exciton-Generation Process Enables Quasi-Planar All-Polymer Organic Solar Cells Exceed 18% Efficiency. *Adv. Funct. Mater.* **2025**, *35* (6), 2414941.
(24) Duan, T.; Feng, W.; Li, Y.; Li, Z.; Zhang, Z.; Liang, H.; Chen, H.; Zhong, C.; Jeong, S.; Yang, C.; Chen, S.; Lu, S.; Rakitin, O. A.; Li, C.; Wan, X.; Kan, B.; Chen, Y. Electronic Configuration Tuning of Centrally Extended Non-Fullerene Acceptors Enabling Organic Solar Cells with Efficiency Approaching 19%. *Angew. Chem., Int. Ed.* **2023**, *62* (42), No. e202308832.
(25) Duan, T.; Wang, J.; Zuo, X.; Bi, X.; Zhong, C.; Li, Y.; Long, Y.; Tu, K.; Zhang, W.; Yang, K.; Zhou, H.; Wan, X.; Zhao, Y.; Kan, B.; Chen, Y. The anti-correlation effect of alkyl chain size on the photovoltaic performance of centrally extended non-fullerene acceptors. *Mater. Horiz.* **2024**, *11* (18), 4413−4423.
(26) White, A. D.; Knight, C.; Hocky, G. M.; Voth, G. A. Communication: Improved *ab initio* molecular dynamics by minimally biasing with experimental data. *J. Chem. Phys.* **2017**, *146* (4), 041102.
(27) Allam, O.; Maghsoodi, M.; Jang, S. S.; Snow, S. D. Unveiling Competitive Adsorption in TiO2 Photocatalysis through Machine-Learning-Accelerated Molecular Dynamics, DFT, and Experimental Methods. *ACS Appl. Mater. Interfaces* **2024**, *16* (28), 36215−36223.
(28) Zou, Z.; Beyerle, E. R.; Tsai, S.-T.; Tiwary, P. Driving and characterizing nucleation of urea and glycine polymorphs in water. *Proc. Natl. Acad. Sci. U.S.A.* **2023**, *120* (7), No. e2216099120.
(29) Caddeo, C.; Fazzi, D.; Caironi, M.; Mattoni, A. Atomistic Simulations of P(NDI2OD-T2) Morphologies: From Single Chain to Condensed Phases. *J. Phys. Chem. B* **2014**, *118* (43), 12556−12565.
(30) Moreno, M.; Casalegno, M.; Raos, G.; Meille, S. V.; Po, R. Molecular Modeling of Crystalline Alkylthiophene Oligomers and Polymers. *J. Phys. Chem. B* **2010**, *114* (4), 1591−1602.
(31) Cheung, D. L.; McMahon, D. P.; Troisi, A. Computational Study of the Structure and Charge-Transfer Parameters in Low-Molecular-Mass P3HT. *J. Phys. Chem. B* **2009**, *113* (28), 9393−9401.
(32) Yuan, J.; Zhang, Y.; Zhou, L.; Zhang, G.; Yip, H.-L.; Lau, T.-K.; Lu, X.; Zhu, C.; Peng, H.; Johnson, P. A.; Leclerc, M.; Cao, Y.; Ulanski, J.; Li, Y.; Zou, Y. Single-junction organic solar cell with over 15% efficiency using fused-ring acceptor with electron-deficient core. *Joule* **2019**, *3* (4), 1140−1151.
(33) Chen, H.; Zou, Y.; Liang, H.; He, T.; Xu, X.; Zhang, Y.; Ma, Z.; Wang, J.; Zhang, M.; Li, Q.; Li, C.; Long, G.; Wan, X.; Yao, Z.; Chen, Y. Lowing the energy loss of organic solar cells by molecular packing engineering via multiple molecular conjugation extension. *Sci. China Chem.* **2022**, *65* (7), 1362−1373.
(34) Abraham, M. J.; Murtola, T.; Schulz, R.; Páll, S.; Smith, J. C.; Hess, B.; Lindahl, E. GROMACS: High performance molecular simulations through multi-level parallelism from laptops to supercomputers. *SoftwareX* **2015**, *1*, 19−25.
(35) Wang, Z.; Li, Z.; Zhang, Y.; Liu, W. Analytic energy gradients of spin-adapted open-shell time-dependent density functional theory. *J. Chem. Phys.* **2020**, *153* (16), 164109.
(36) Liu, W.; Hong, G.; Dai, D.; Li, L.; Dolg, M. The Beijing four-component density functional program package (BDF) and its application to EuO, EuS, YbO and YbS. *Theor. Chem. Acc.* **1997**, *96*, 75−83.
(37) Zhang, Y.; Suo, B.; Wang, Z.; Zhang, N.; Li, Z.; Lei, Y.; Zou, W.; Gao, J.; Peng, D.; Pu, Z.; Xiao, Y.; Sun, Q.; Wang, F.; Ma, Y.; Wang, X.; Guo, Y.; Liu, W. BDF: A relativistic electronic structure program package. *J. Chem. Phys.* **2020**, *152* (6), 064113.
(38) Liu, W.; Wang, F.; Li, L. The Beijing density functional (BDF) program package: methodologies and applications. *J. Theor. Comput. Chem.* **2003**, *02* (02), 257−272.
(39) Liu, W.; Wang, F.; Li, L. Relativistic density functional theory: The BDF program package. *Recent Adv. Comput. Chem.* **2004**, *5*, 257−282.
(40) Hess, B.; Bekker, H.; Berendsen, H. J.; Fraaije, J. G. LINCS: A linear constraint solver for molecular simulations. *J. Comput. Chem.* **1997**, *18* (12), 1463−1472.
(41) Parrinello, M.; Rahman, A. Polymorphic transitions in single crystals: A new molecular dynamics method. *J. Appl. Phys.* **1981**, *52* (12), 7182−7190.
(42) Nosé, S. A unified formulation of the constant temperature molecular dynamics methods. *J. Chem. Phys.* **1984**, *81* (1), 511−519.
(43) Humphrey, W.; Dalke, A.; Schulten, K. VMD: visual molecular dynamics. *J. Mol. Graph.* **1996**, *14* (1), 33−38.
(44) Michaud-Agrawal, N.; Denning, E. J.; Woolf, T. B.; Beckstein, O. MDAnalysis: a toolkit for the analysis of molecular dynamics simulations. *J. Comput. Chem.* **2011**, *32* (10), 2319−2327.
(45) Niu, Y.; Li, W.; Peng, Q.; Geng, H.; Yi, Y.; Wang, L.; Nan, G.; Wang, D.; Shuai, Z. MOlecular MAterials Property Prediction Package (MOMAP) 1.0: a software package for predicting the luminescent properties and mobility of organic functional materials. *Mol. Phys.* **2018**, *116* (7−8), 1078−1090.
(46) Nan, G.; Yang, X.; Wang, L.; Shuai, Z.; Zhao, Y. Nuclear tunneling effects of charge transport in rubrene, tetracene, and pentacene. *Phys. Rev. B: Condens. Matter Mater. Phys.* **2009**, *79* (11), 115203.
(47) Shuai, Z.; Wang, D.; Peng, Q.; Geng, H. Computational Evaluation of Optoelectronic Properties for Organic/Carbon Materials. *Acc. Chem. Res.* **2014**, *47* (11), 3301−3309.
(48) Shuai, Z.; Geng, H.; Xu, W.; Liao, Y.; André, J.-M. From charge transport parameters to charge mobility in organic semiconductors through multiscale simulation. *Chem. Soc. Rev.* **2014**, *43* (8), 2662−2679.
(49) Valeev, E. F.; Coropceanu, V.; da Silva Filho, D. A.; Salman, S.; Brédas, J.-L. Effect of Electronic Polarization on Charge-Transport Parameters in Molecular Organic Semiconductors. *J. Am. Chem. Soc.* **2006**, *128* (30), 9882−9886.
(50) Zhu, W.; Spencer, A. P.; Mukherjee, S.; Alzola, J. M.; Sangwan, V. K.; Amsterdam, S. H.; Swick, S. M.; Jones, L. O.; Heiber, M. C.; Herzing, A. A.; Li, G.; Stern, C. L.; DeLongchamp, D. M.; Kohlstedt, K. L.; Hersam, M. C.; Schatz, G. C.; Wasielewski, M. R.; Chen, L. X.; Facchetti, A.; Marks, T. J. Crystallography, Morphology, Electronic Structure, and Transport in Non-Fullerene/Non-Indacenodithienothiophene Polymer:Y6 Solar Cells. *J. Am. Chem. Soc.* **2020**, *142* (34), 14532−14547.

https://doi.org/10.1021/acsami.5c08785
ACS Appl. Mater. Interfaces 2025, 17, 45947−45957